Materials Science & Engineering A 831 (2022) 142234

Contents lists available at ScienceDirect

Materials Science & Engineering A

journal homepage: www.elsevier.com/locate/msea

Additively manufactured Haynes 282: effect of unimodal vs. bimodal γ'-microstructure on mechanical properties

Reza Ghiaasiaan [a,b], Nabeel Ahmad [a,b], Paul R. Gradl [c], Shuai Shao [a,b], Nima Shamsaei [a,b,*]

[a] Department of Mechanical Engineering, Auburn University, Auburn, AL36849, USA
[b] National Center for Additive Manufacturing Excellence NCAME, Auburn University, Auburn, AL, 36849, USA
[c] NASA Marshall Space Flight Center, Propulsion Department, Huntsville, AL, 35812, USA

ARTICLE INFO

Keywords:
Laser powder bed fusion (L-PBF or LB-PBF)
Additive manufacturing
Ni-base superalloy
Heat treatment
Microstructure
Tensile properties

ABSTRACT

This study examines the effects of lower-than-nominal heat treatment (HT) temperatures and cooling rates —possible during the treatment of larger components— on microstructure and tensile properties Haynes 282 manufactured via laser powder bed fusion (L-PBF) additive manufacturing process. Two main HT schedules, i.e., conventional treatment and its lower temperature variants were performed. The microstructural evolution at each step of the HTs was tracked and compared. It was shown that solution temperature of a wide range (1062–1146 °C) could moderately remove the as-solidified dendritic microstructure resulting in similar distribution of grain boundary (GB) carbides. In addition, the lower temperature double aging process resulted in a bimodal γ′-precipitates consisting of both nano-sized secondary γ'- and large primary (>~100 nm) γ′-precipitates, while the conventional aging gave rise to a unimodal γ′-precipitates with precipitates of diameter ~60 nm. Owing to the bimodal γ′-precipitates and a similar GB carbide distribution, the low temperature HTs resulted in comparable tensile properties to the conventional HT despite having much larger γ′-precipitates. The results imply that moderate HT temperature deviations due to excessive component size, such as lower temperatures and slower heating/cooling rates, does not negatively impact the mechanical properties of L-PBF Haynes 282.

1. Introduction

Additive manufacturing (AM) shows a promising and growing interest in industries, such as aerospace, biomedical, energy, and automotive [1–6]. Its capability of fabricating net-shaped parts with complex geometries may substantially reduce production costs for some hard-to-machine alloys whose applications demand unique shapes, such as Ni-base superalloys used for blades/disks in gas turbines. AM's net-shaping capability can also enable the consolidation of many parts into one integral component. The prime examples in aerospace include the fuel nozzle for GE's LEAP engine [7] and the Pogo Z-baffle for NASA's RS-25 rocket engine [8,9]. However, compared to individual small parts, the consolidated components have larger size and added mass, which may decrease the heating/cooling rates between consecutive steps and maximum reachable temperatures during multistep heat treatments (HT), potentially resulting in a nonuniform microstructure throughout the component.

The strength in γ-γ' Ni-base alloys, such as the Haynes 282 alloy, is primarily derived from the precipitation of γ' phase within grains and additionally by solid solution and the carbide precipitation at grain boundaries (GB) [10,11]. While the size, morphology, and distribution of γ′-phases [10,12,13] can govern both the static strength as well as creep behavior of these alloys in both single- and poly-crystalline forms, grain size and GB carbides are important for their creep properties in the polycrystalline form [14]. Therefore, properly designed and controlled HT has always been very important as they determine the type, size, distribution, and morphology of such microstructural constituents in Ni-base alloys [15–19]. The properly designed HT is even more crucial for additively manufactured (AM) components as the efficacy of conventional HT in achieving peak mechanical properties may be compromised by the process-induced microstructural characteristics such as micro-segregation [20] which may be further exacerbated by the potentially larger component size.

The conventional HT of Haynes 282 designed for the rolled sheet and plate forms consists of solutionizing between 1121 °C and 1149 °C for about 1 h followed by a two-step aging HT at 1010 °C for 2 h, air cool, plus 788 °C/8 h air cool [10,21–26]. During the solution treatment, the

* Corresponding author. Department of Mechanical Engineering, Auburn University, Auburn, AL36849, USA.
E-mail address: shamsaei@auburn.edu (N. Shamsaei).

https://doi.org/10.1016/j.msea.2021.142234
Received 27 July 2021; Received in revised form 23 September 2021; Accepted 21 October 2021
Available online 23 October 2021

Abbreviations and nomenclature

1062wLA	Solutioned at 1062 °C/1 h and aged at 979 °C/2 h + 757 °C/8 h
1104wLA	Solutioned at 1104 °C/1 h and aged at 979 °C/2 h + 757 °C/8 h
1118wLA	Solutioned at 1118 °C/1 h and aged at 979 °C/2 h + 757 °C/8 h
1135wCA	Solutioned at 1135 °C/1 h and aged at 1010 °C/2 h + 788 °C/8 h
1146wLA	Solutioned at 1146 °C/1 h and aged at 979 °C/2 h + 757 °C/8 h
1062wNo	Only solutioned at 1062 °C/1 h
1104wNo	Only solutioned at 1104 °C/1 h
1118wNo	Only solutioned at 1118 °C/1 h
1135wNo	Only solutioned at 1135 °C/1 h
1146wNo	Only solutioned at 1146 °C/1 h
AM	Additive manufacturing/Additively manufactured
BSE	Backscattered electron
EBSD	Electron backscatter diffraction
EDM	Electrical discharge machining
EDS	Energy dispersive spectroscopy
EL	Elongation to failure
GB	Grain boundary
HT	Heat treatment/Heat treatments/Heat treated
ICP	Inductively coupled plasma
IPF	Inverse pole figure
L-PBF	Laser powder bed fusion
LP-DED	Laser powder direct energy deposition
NHT	Non-heat treated
SEM	Scanning electron microscope/Scanning electron microscopy
UTS	Ultimate tensile strength
YS	Yield strength
M_6C	Metal carbide: often Mo-rich, forming at ~816 to 982 °C
$M_{23}C_6$	Metal carbide: often Cr-rich, forming at ~790 to 816 °C
MC	Metal carbide: often Ti-rich, forming at ~1200 to 1260 °C
γ	Gamma phase with an FCC lattice
γ'	Gamma prime phase with an L12 lattice

γ'-phase dissolves and primary high temperature Ti-rich (MC) carbides (forming at ~1200–1260 °C) are transformed partially into the secondary low/medium temperature carbides such as the Cr-rich ($M_{23}C_6$) carbides (forming at ~790–816 °C) and Mo-rich (M_6C) carbides (forming at ~816–982 °C) at GB [10]. Furthermore, during the first step of aging, which is sometimes referred to as the "stabilization" treatment, more secondary carbides precipitate at GB. Subsequently, during the second step aging, a unimodal microstructure of fine, spherical γ'-phases with uniform distribution within grain interiors is formed [10,18].

Dictated by the unique thermal history of AM processes [10,27,28], the typical dendritic as-solidified microstructures of AM Haynes 282 not only differ from those of the mill-annealed condition but also can vary significantly among different AM techniques. For instance, although both of the laser and electron beam-based AM processes are associated with high cooling rates [29], the build plate during the electron beam powder bed fusion (EB-PBF) process typically reaches a very high temperature (900–1000 °C), which can result in a much more homogenized microstructure compared to the laser powder bed fusion (L-PBF) [23,30]. Although conventional HT has been routinely applied to Haynes 282 in various AM forms such as EB-PBF [23,24] Laser Powder Directed Energy Deposition (LP-DED) [31–33] and L-PBF [34–36], two primary questions remain: (a) can the HT applied to AM materials result in similar microstructure as wrought? and (b) would a lower-than-nominal temperature and heating/cooling rates, caused by larger and more complex geometries, negatively impact the mechanical property?

Existing knowledge on wrought Haynes 282 suggests that slightly lower first step aging temperature may induce bi-modal γ'-precipitates which can improve ductility without sacrificing strength. For instance Joseph et al. [12]. reported a presence of γ'-precipitates at two sizes of 130 nm and 50 nm after a low temperature 2-step aging at 996 °C (roughly the solvus temperature for the γ'-phases), followed by furnace cooling to the conventional second aging at 788 °C and 8 h of isothermal holding. Outcome of lower temperatures in both aging steps is presently not well known.

In addition, the bi-modal microstructure has not been observed in L-PBF Haynes 282 subjected to similar treatment. Recently, Christofidou et al. [34] studied the microstructure of L-PBF Haynes 282 using low temperature 2-step aging at 900 and 990 °C (which are below the solvus temperature of γ'-precipitates) for the first step of aging, followed by the conventional second step aging at 788 °C for 8 h. They reported a unimodal γ'-microstructure for both low temperatures during first step of aging, but with larger γ'-precipitates of 93 ± 34 nm and 105 ± 43 nm, respectively. Similarly, and more recently, Deshpande et al. [35] studied the L-PBF Haynes 282 using a lower temperature 2-step aging of 1000 °C for 2 h, followed by 8 h at 788 °C. They also reported a unimodal γ'-microstructure with slightly larger γ'-particles (~60 nm).

The objective of the present work is to understand the effect of both conventional heat treatment as well as its lower-temperature variants on the microstructure and mechanical properties of the L-PBF Haynes 282 alloy. The effect of solution temperature in the range of 1062–1146 °C on removing the as-solidified dendritic microstructure is also investigated. The conventional heat treatment includes a solution step at 1135 °C for 1 h, aging at 1010 °C for 2 h followed by air cooling, and aging at 788 °C for 8 h. The lower temperature heat treatment variants constitute solution treatments at 1062–1146 °C for 1 h followed by aging at 979 °C (which is below γ'-solvus temperature) for 2 h followed by furnace cool (FC) to 757 °C and isothermal hold time for 8 h followed by air cooling. This article is organized as the following: *Section 2* presents the materials and experimental procedures used for this study such as HT, test specimens, and characterization (both mechanical and microstructural) methodologies; *Section 3* includes experimental results; *Section 4* discusses the experimental observations. Finally, a brief concluding summary is presented in *Section 5*.

2. Experiments and materials

The test specimens for this study were fabricated into net shapes with no additional surface machining using a L-PBF technology by Carpenter Additive, Athens, AL. The fabricated specimens were removed from the built plate using wire electrical discharge machining (EDM). Note that the detailed L-PBF process parameters are considered proprietary by the manufacturer (Carpenter Additive), and therefore, are not disclosed here. The chemical composition of the Haynes 282 powder measured using the inductively coupled plasma (ICP) spectroscopy and X-ray fluorescence is presented in Table 1. The powder particles were specified to be within the 15–45 μm size range. The powder chemistry and size distribution were provided by the manufacturer (Carpenter Additive).

2.1. Heat treatment procedures

Two main heat treatment schedules were performed in this study, namely, the conventional one, typically used for wrought Haynes 282, and the low temperature variants. The conventional heat treatment comprises a solution step at 1135 °C/1 h, aging at 1010 °C/2 h followed

Table 1
Nominal and measured composition of Haynes 282 powder used for this study.

wt.%	Ni	Cr	Mo	Co	Ti	Al	Fe	Ta	Nb
Nominal	Balance	18.5–20.5	8-9<	9–11	1.9–2.3	1.36–1.65	0–1.5	0–0.1	0–0.2
Measured	57.3	19.7	8.6	10.5	2.2	1.6	<0.1	–	–

by air cooling (cooling rate >8 °C/min), and aging at 788 °C/8 h. The low temperature variants constitute a range of solution temperature from 1062 °C to 1146 °C followed by aging temperatures that are ~30 °C lower than nominal temperatures and slower furnace cooling (2.8 °C/min) in between. The test specimens were heat treated (HT) using a SENTRO TECH high-temperature tube furnace (Strongsville, OH) in an Ar atmosphere using an external thermocouple attached to them during heat treatment.

Table 2 lists the details of procedures along with the designation convention used in this study for each heat treatment schedule. Specifically, a HT procedure is designated sequentially according to the solution treatment (first four digits as the solutionizing temperature), cooling media (next letter), and aging steps (last two letters) performed. For instance, *1062wLA* stands for solutioning at 1062 °C for 1 h, water quenched (*w*), and followed by a low temperature double aging (*LA*) process. It should be noted that all specimens were HT using the low temperature double aging (979 °C/2 h + furnace cool + 757 °C/8 h + air cool) except for the specimens solutioned at 1135 °C which were HT using the conventional 2-step aging procedure (1010 °C/2 h + air cool + 788 °C/8 h + air cool). Solution-only treatments were also applied to examine the efficacy of various solution temperatures in removing the as-solidified dendritic microstructure.

2.2. Test specimens and mechanical testing

The uniaxial tensile specimens were additively manufactured into the final dimensions according to ASTM E8 as shown in Fig. 1(a) [37]. The tensile specimens were tested in the as-built surface condition, without any further surface treatment. The uniaxial tensile tests were performed according to the ASTM-E8 standard [37] with a displacement rate of 0.012 mm/s (0.001/s nominal strain rate). The tests were displacement controlled with the initial stages (first 0.050 mm/mm strain) being carried out with the extensometer for accurate calculation of yield strength. Note that the tensile properties reported in this study are the mean values obtained over at least three tests.

2.3. Metallography and microscopy

Microstructural samples were cut off from the witness specimens with 13.8 mm diameter and 86.4 mm height using an abrasive cutter as shown in Fig. 1(b). The microstructural studies were performed on the x-y plane. The mounted specimens were then ground and polished using EcoMet TM 30 Semi-Automatic Grinder Polisher (Buehler Materials, Lake Bluff, IL). Metallography procedures were carried out according to the ASTM-E3 standard [38]. They were first ground using 220, 320, 400, and 600 grit silicon carbide (SiC) papers with light contact pressure to obtain a planar surface free from deep grooves. The polishing procedure was then performed using 0.05 μm colloidal silica with water.

Scanning electron microscopy (SEM) was performed on the x-y plane of microstructural samples using a Zeiss Crossbeam 550 Scanning Electron Microscope (SEM) (Zeiss Group). Electron Channeling Contrast Imaging [39] was conducted using the four-quadrant backscattered electron detector. Further, the energy dispersive x-ray spectroscopy (EDS) and electron backscatter diffraction (EBSD) analyses were performed using the Oxford instruments onboard the microscope.

Table 2
List of heat treatment designations used for this study. Solution treatment was 1 h for all conditions. A 2-step low temperature double aging stipulates a 2 h isothermal hold time at 979 °C followed by furnace cooling to 757 °C and 8 h isothermal hold time; while a conventional double aging stipulates a 2 h isothermal hold time at 1010 °C followed by air cooling to 788 °C and 8 h isothermal hold time.

Solution Treatment (1 h)		Aging Treatment	Designation
Temperature (°C)	**Quenching Rate**		
1062	Water (*w*)	None (*No*)	*1062wNo*
		Low Temp. (*LA*)	*1062wLA*
1104	Water (*w*)	None (*No*)	*1104wNo*
		Low Temp. (*LA*)	*1104wLA*
1118	Water (*w*)	None (*No*)	*1118wNo*
		Low Temp. (*LA*)	*1118wLA*
1135	Water (*w*)	None (*No*)	*1135wNo*
		Conv. Temp. (*CA*)	*1135wCA*
1146	Water (*w*)	None (*No*)	*1146wNo*
		Low Temp. (*LA*)	*1146wLA*

3. Experimental results

3.1. Uniaxial tensile properties

Uniaxial tensile properties, including the engineering stress-displacement curves and a comparative bar graph of L-PBF Haynes 282 superalloy subjected to various heat treatment conditions, are presented in Fig. 2. As shown, solution treatment temperature does not seem to have a significant effect on the uniaxial tensile properties of the low temperature treated specimens. Indeed, not only the stress-displacement curves of *1118wLA*, *1104wLA*, and *1062wLA* specimens closely follow each other (Fig. 2(a)), but the measured yield strength (YS), ultimate tensile strength (UTS), and elongation to failure (EL) are also very similar (Fig. 2(b)). It is notable from Fig. 2 that the tensile properties of the conventional and low temperature treated specimens seem to be quite comparable. While the YS of the low temperature treated specimens are moderately lower (by ~100 MPa), their UTS and EL are somewhat identical to the ones processed by conventional treatment.

Further, the tensile results of the L-PBF Haynes 282 obtained in this study are compared in Fig. 3 with the other AM and wrought counterparts obtained from the literature [12,13,21,23,31,32,34–36,40] in both conventionally HT and the low temperature 2-step aged conditions (996 °C/2 h/FC + 788 °C/8 h/AC) [12]. As shown, the tensile properties obtained in this study are quite comparable to those obtained for other AM and wrought counterparts in similar HT conditions. A consistent trend observed among all data is that Haynes 282 is more ductile behaving in the NHT conditions, while having lower YS and UTS. However, a significant enhancement in YS and UTS can be obtained by applying HT at the cost of reduction in EL.

3.2. Microstructure

The microstructural features of the Haynes 282 in non-heat treated (NHT), solutioned only, and solutioned + aged conditions are presented in Fig. 4. Inverse pole figure (IPF) maps and BSE micrographs obtained from the x-y plane of the NHT as well as various solution treated (not aged) specimens are presented in Fig. 4(a)–(l). As shown, the sub-granular structures and a clear dendritic characteristic within the grains persist even after solutionizing, although they do become less discernible with increasing solution temperature. The particle-like features in Fig. 4(h)–(l) were further examined by EDS scans (an example is

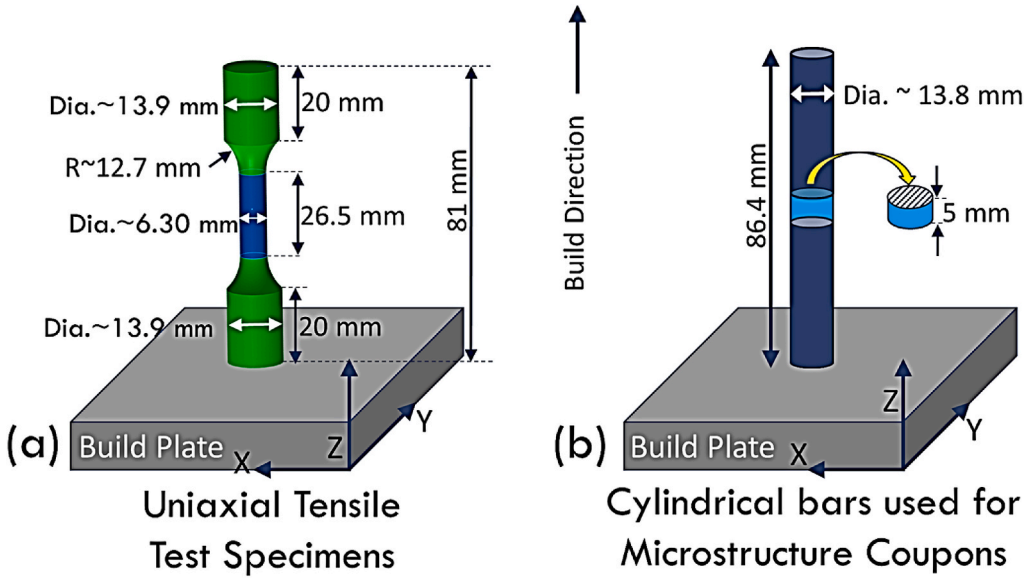

Fig. 1. Schematics showing (a) the geometry of the uniaxial tensile specimens used for this study according to the ASTM-E8 standard; and (b) a typical cylindrical bar used for cutting microscopy samples.

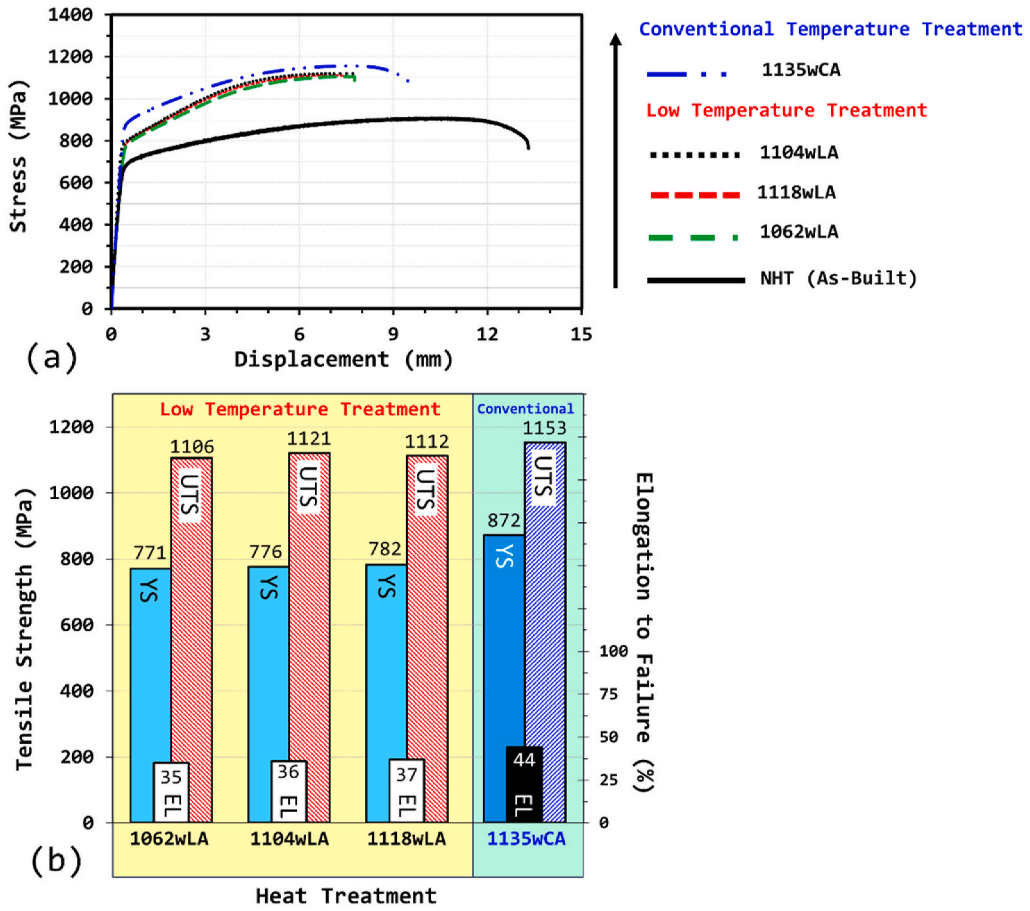

Fig. 2. Uniaxial tensile properties obtained in this study for L-PBF Haynes 282 in various HT/non-heat treated (NHT) conditions: (a) engineering stress-displacement curves and (b) comparative bar chart for yield strength (YS), ultimate tensile strength (UTS), and elongation to failure (EL).

shown in Fig. 5) and were determined to be carbides and nano-scale pores. The carbides and nanopores are marked by an arrow in red and white in Fig. 4, respectively.

The very small dark specs in Fig. 4(g) are γ' precipitates, which are evident from Fig. 4(m) under higher magnification. While precipitation does not readily occur during solidification, the unique layer-by-layer fabrication strategy of L-PBF induced repeated reheating which essentially created an "aging" condition for some precipitates to form. These

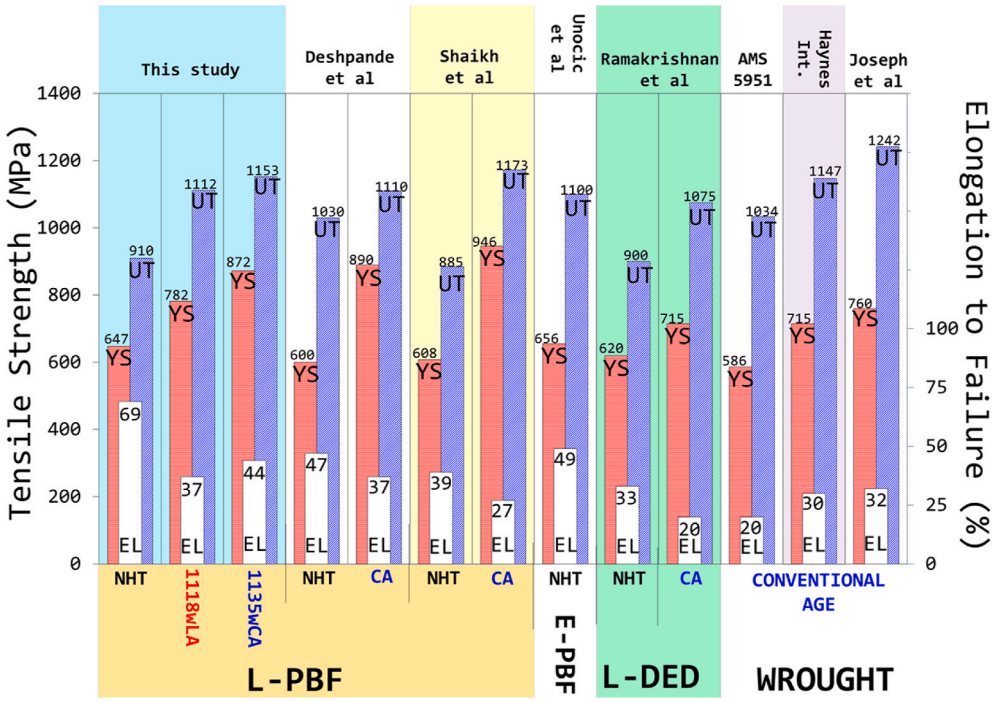

Fig. 3. Comparative bar chart for the room temperature uniaxial tensile properties: YS, UTS, and EL obtained in this study for Haynes 282 manufactured by L-PBF with the other AM and wrought counterparts obtained from literature in two different HT.

as-fabricated γ' precipitates were dissolved during the solution treatments (see Fig. 4(h)–(l)). The high magnification BSE micrographs Fig. 4 (n)–(r) present the γ' precipitation structure in both NHT and aged conditions. After lower temperature aging (*1062wLA* through *1146wLA*), relatively large precipitates with a mean diameter ~130 ± 25 nm were formed despite the different solution temperatures. On the other hand, the conventional aging generated much smaller precipitates (mean diameter ~69 ± 11 nm).

The results of grain size measurements obtained from EBSD analysis (shown in Fig. 4(a)–(f)) are presented in Table 3 for all heat treatment conditions. As shown, significant variation in grain size exists in each heat treatment condition which is common for AM processed metallic materials [23,31]. For instance, the grain size of the NHT L-PBF Haynes 282 varies between 4–184 μm. However, despite some degree of grain growth that has occurred during different HT, the grain sizes were not significantly affected by different solution temperatures. The mean values of equivalent circular grain diameter vary from 14.3 μm (ASTM # 9 [41]) in *1062wNo* condition to 34 μm (ASTM # 7) in *1146wNo* condition, which could be attributed to the pinning effect of carbides, forming during solution treatment at GB and within grain interiors, on the grain growth [10]. Examples of GB carbides are shown in the high magnification BSE micrographs in Fig. 4 (i)–(l). In comparison, for the conventionally manufactured Haynes 282, the average grain size has been reported to be between 55 μm [42] (ASTM # 5) and 120 μm [21] (ASTM # 3), depending on solution treatment temperature, i.e., the higher the solution treatment; the larger the size of grains.

As shown by the typical elemental mapping results along with the X-ray spectrum for one of the HT (*1104wLA*) in Fig. 5, the GBs of the L-PBF specimens fabricated in this study are decorated by carbides, which persisted through the HT. The carbide phases are visible in the micrographs forming at the grain boundaries (marked by the arrows in Fig. 5 (a)). These carbide phases could be either the high temperature primary Ti-rich (MC) carbides (forming at ~1200–1260 °C) as well as the secondary medium temperature Mo-rich (M_6C) carbides (forming at ~816–982 °C) and secondary low temperature Cr-rich ($M_{23}C_6$) carbides (forming at ~790–816 °C) that have been formed and/or transformed, respectively, during solution and/or aging steps [10].

4. Discussion on experimental results

4.1. Influence of heat treatment temperature on tensile behavior

In the NHT condition, although some γ' precipitates formed (see Fig. 4), both their size and volume fraction are far from the peak aged condition due to the inadequate thermo exposure time during fabrication. The resulting strengths are, therefore, substantially lower than the fully HT conditions (see Fig. 2(a)). On the other hand, both the conventional and low temperature HT specimens yielded very similar tensile responses. The small differences mainly reside in the YS. Specifically, the *1118wLA*, *1104wLA*, and *1062wLA* specimens yielded ~100 MPa lower than the *1135wCA* specimens. The slightly lower YS can be ascribed to the presence of large (>150 nm) primary γ' precipitates in the low temperature treated specimens, while the ones in the *1135wCA* are on average ~60 nm in diameter. Assuming the same volume fraction of γ', larger precipitates have larger inter-precipitate spacing, permitting easy dislocation bowing, and thus resulting in lower flow stress, i.e. [43–45], $\tau = \frac{\alpha G b}{d}$, where τ is the resolved shear flow stress, α is a factor that accounts for the dislocation line tension, G is the shear modulus, and b is the magnitude of the Burgers vector. The average distance (*d*) between larger precipitates, for the low temperature treated specimens, is of the order of 300 nm, while that for the conventionally treated specimens is ~100 nm. Solely based on the strengthening of the primary precipitates, the yield strength for *1135wCA* specimens is expected to be three times higher than the *1118wLA*, *1104wLA*, and *1062wLA* specimens, which is inconsistent with the data presented in Fig. 2.

The discrepancy between the expectation and the measured YS could be explained by the significant contribution from other strengthening sources, including solid solution, secondary precipitate, and grain size. Among the three sources, the grain size was not affected by the heat treatment conditions utilized in this study. In addition, the degree of solid solution mainly depends on the solution temperature and, given the relatively small solution temperature range probed (1062–1146 °C), its effect is not expected to be a dominating factor on strength. This is further confirmed by comparing the YS of the fully aged specimens.

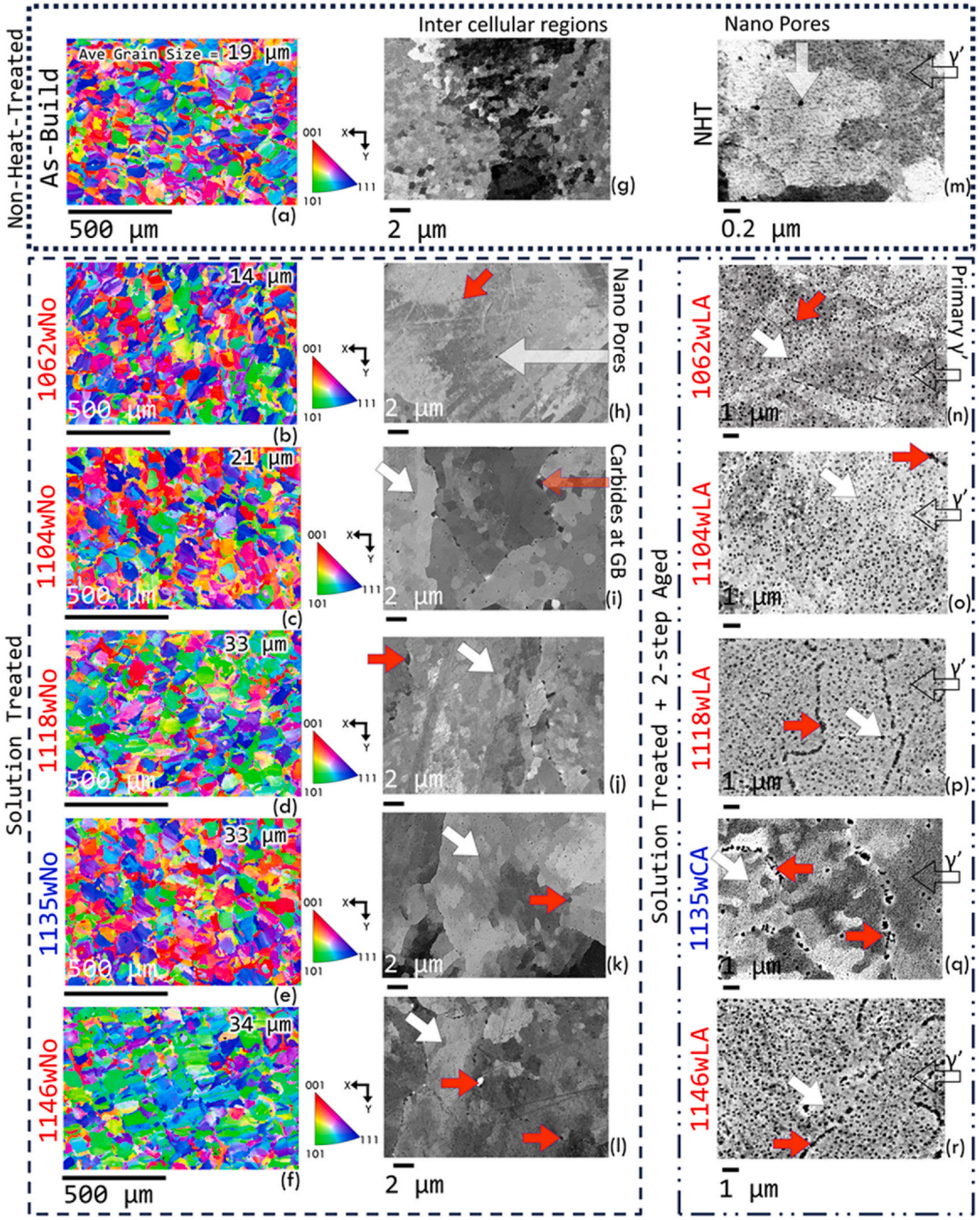

Fig. 4. Typical IPF maps from EBSD scans and BSE SEM micrographs obtained using ECCI for various solution treated conditions including *NHT*, *1062wNo*, *1104wNo*, *1118wNo*, *1135wNo,* and *1146wNo* along with the respective fully aged conditions. Specific conditions of the micrographs are also marked in the figure.

Fig. 2 shows that the YS for the *1118wLA* condition is closer to that of the *1062wLA*, instead of *1135wCA*, even though the solution temperature of the latter is more similar, which suggests a bigger influence posed by aging (i.e., LA vs. CA) than solution temperature. The remaining source is the possible existence of smaller, secondary precipitates.

Closer inspection of the lower temperature treated microstructures at higher magnifications indeed revealed that the presence of secondary γ' precipitates that are much smaller in size (<20 nm). Fig. 6(a)-(c) present high magnification BSE images of microstructures in *1062wLA*, and *1104wLA*, and *1118wLA* conditions, respectively. In contrast, the microstructure in 1135wCA condition is unimodal and free of such small secondary precipitates (see Fig. 6(d)). As shown in Fig. 6(a)–(c), the microstructures induced by the low temperature HT resulted in bimodal microstructures containing large precipitates that are relatively far apart (~300 nm) with small precipitates filling the space between. The spacing between the secondary γ' precipitates is very small (well below 50 nm), which can significantly impede the glissile motion of dislocations and improve strength. The bimodal γ'-microstructure is likely the reason for the YS of the *1118wLA*, *1104wLA*, and *1062wLA* specimens not being significantly lower than that of the *1135wCA* ones despite the presence of large primary precipitates.

After yielding, the strain hardening rates for the low temperature treated specimens are slightly higher than those of the conventionally treated specimens (see Fig. 2(a)). This is consistent with the high number density of the secondary precipitates present in the low temperature specimens (see Fig. 6(a)–(c)), which promotes dislocation

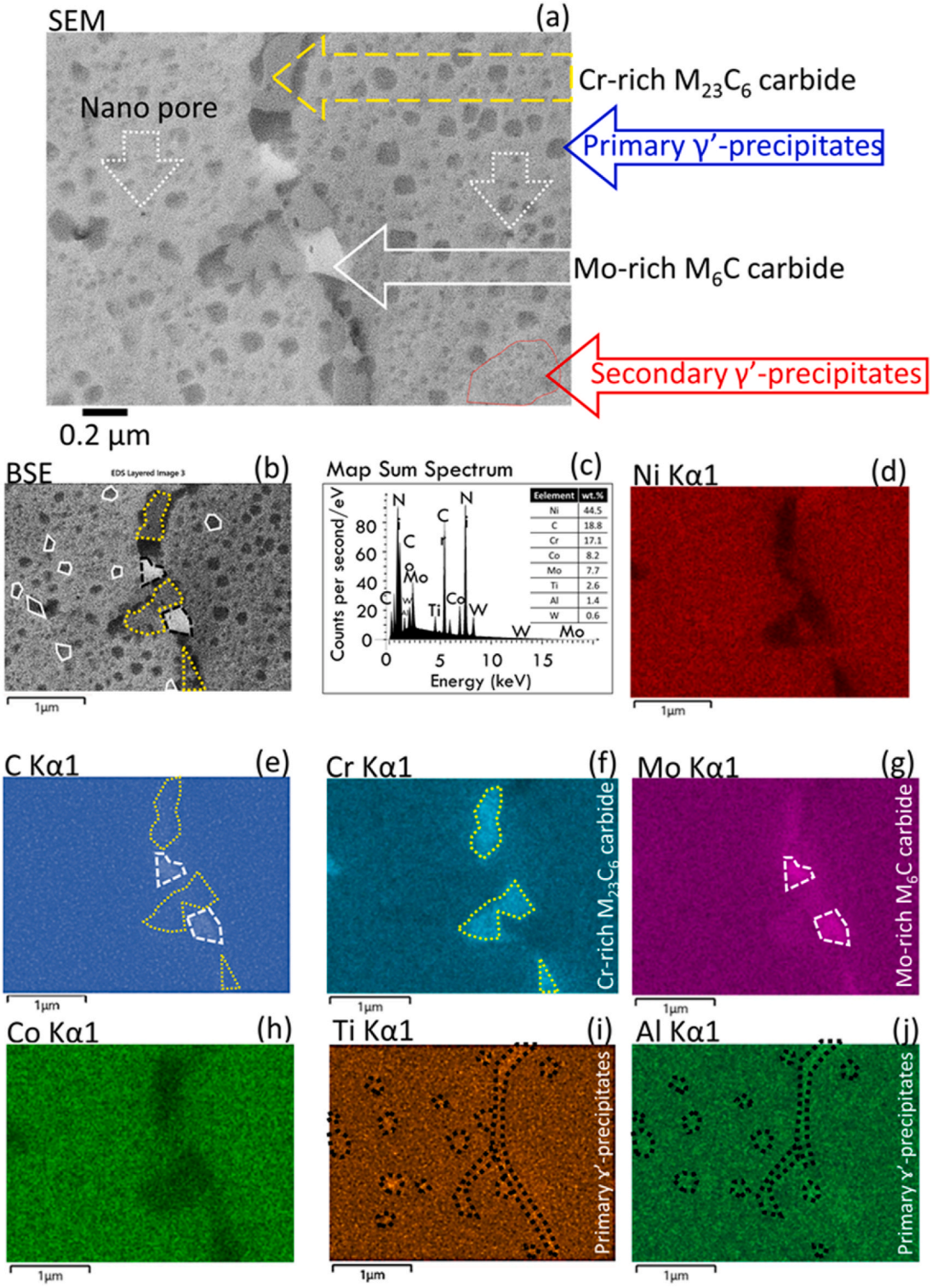

Fig. 5. Typical EDS elemental mapping for *1104wLA*; (a) SEM micrograph, (b) BSE micrograph, (c) X-ray spectrum from the scanned area for each element showing the primary carbides forming at grain boundary areas; (d)–(j) elemental mapping for each element found in the EDS detection list.

reaction and multiplication. As a result, even though these specimens had lower YS, their UTS is similar to the conventionally treated ones.

The similar EL among specimens processed by all HT may be ascribed to their similar GB carbide dominated fracture mechanism. Tensile fracture surfaces of a *1104wLA* specimen and a *1135wCA* specimen are presented in Fig. 7. As can be seen in Fig. 7(a) and (d), both fracture surfaces comprise a central fibrous region, surrounded by a semi-"conical" region forming a 45° angle with the loading axis, which resembles the well-known cup-and-cone feature [46]. The cup-and-cone fracture mechanism begins with the nucleation, growth, and coalescence of voids which is followed by the rapid symmetrical propagation of the crack in plane strain condition from center to the surface and concludes by the final shear off in plane stress near specimen surface. The nucleation and growth phases of the crack leave a fibrous region in

Table 3
The grain size resulting from various heat treatment procedures listed in Table 2. The grain size was measured from IPF maps shown in Fig. 4.

Temper	Solution Temperature	Grain Size (μm)			
	(°C)	Ave.	STDEV	Min.	Max.
NHT	**NA**	19	±21	4.3	143
1062wNo	**1062**	14	±17	4.5	131
1062wLA		15	±18	4.6	81
1104wNo	**1104**	21	±18	6.1	99
1104wLA		23	±17	7.7	136
1118wNo	**1118**	33	±19	15	136
1118wLA		30	±17	15	127
1135wNo	**1135**	31	±20	16	125
1135wCA		32	±18	15	129
1146wNo	**1146**	34	±19	15	130
1146wLA		34	±19	15	125

the center of the fracture surface, while the shear off phase leaves an annular shear lip.

The nucleation-growth-coalescence of voids leaves dimples in the central regions of the fracture surface which are visible in the high magnification micrographs in Fig. 7(c) and (f). In materials free of apparent defects such as porosity or second phase particles, the nucleation of voids typically occurs near dislocation pileups which leads to a more homogeneous distribution of dimples in the fibrous region of the fracture surface. For the L-PBF Haynes 282 investigated in this work, microscopic cracks—coexisting with the dimples—are also evident on the fracture surfaces of both the conventionally and the low temperature treated specimens (such as the ones shown in Fig. 7(b) and (e)). As seen, these cracks appear to be along the loading direction, i.e., perpendicular to the fracture surfaces and have morphology resembling the GB as shown in Fig. 4.

The origins of the microcracks are further examined via the BSE microscopy performed on the longitudinal polished cross sections of the fractured specimens. Micrographs of two of such specimens, i.e., one that was treated by *1135wCA* condition and the one treated by the *1118wLA* condition, are presented in Fig. 8. As is evident from Fig. 8(a), (b), (e), and (f), the micro cracks were indeed nucleated from the carbide residing on the GBs. Further, the crack nucleation appears to be caused by the debonding of the interface between carbides and γ matrix (see Fig. 8(c), (d), (g), and (h)). Again, similar void and crack nucleation mechanisms were observed for both the conventionally and low temperature HT specimens.

4.2. The formation of bimodal γ' microstructure

As shown by BSE micrographs in Fig. 4 (third column), the final microstructures of both the conventional and low temperature HT consisted of the γ-matrix, γ'-precipitates and carbides. However, higher magnification images in Fig. 6 also clearly revealed that the low temperature treatments (i.e., *1062wLA*, *1104wLA*, and *1118wLA*) resulted in a bimodal γ'-microstructure with two distinctive precipitate sizes; where the primary precipitates are >∼150 nm in diameter and the secondary precipitates are ∼ 10–20 nm in diameter. On the other hand, the *1135wCA* treatment resulted in the unimodal γ'-microstructure where the precipitate sizes are relatively uniform and ∼60 nm in diameter (see Fig. 6(d)).

To identify the origins of bimodal γ' microstructure formed as the result of low temperature HT, the microstructural evolutions of L-PBF Haynes 282 alloy during multiple stages of the conventional heat treatment (*1135wCA*: solution 1135 °C/1 h + water quench + aging 1010 °C/2 h + air cool + aging 788 °C/8 h + air cool), and the low temperature heat treatment (*1118wLA*: solution 1118 °C/1 h + water quench + aging 979 °C/2 h + furnace cool + aging 757 °C/8 h + air cool) are presented and compared in Fig. 9. Note that the BSE micrographs were obtained from the fast quenched specimens immediately

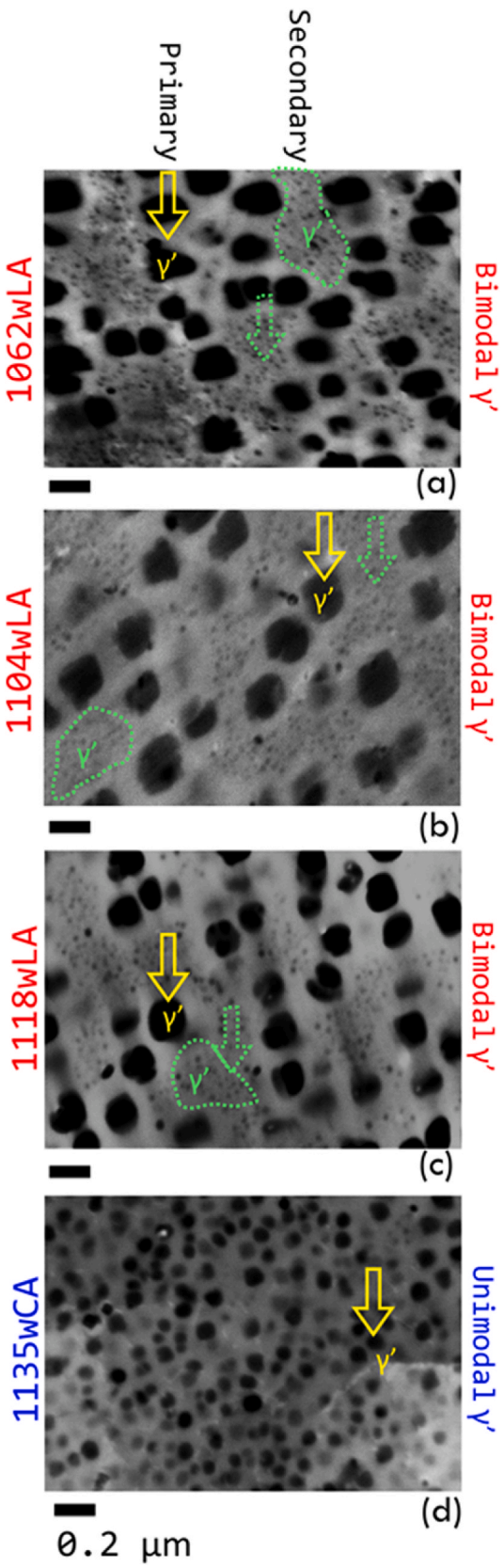

Fig. 6. High magnification BSE micrographs showing the bimodal and unimodal γ' microstructures resulted from (a) *1062wLA*, (b) *1104wLA*, (c) *1118wLA*, and (d) *1135wCA* HT. Yellow arrows indicate primary γ' precipitates, green arrow and enclosures indicate secondary ones. (For interpretation of the references to colour in this figure legend, the reader is referred to the Web version of this article.)

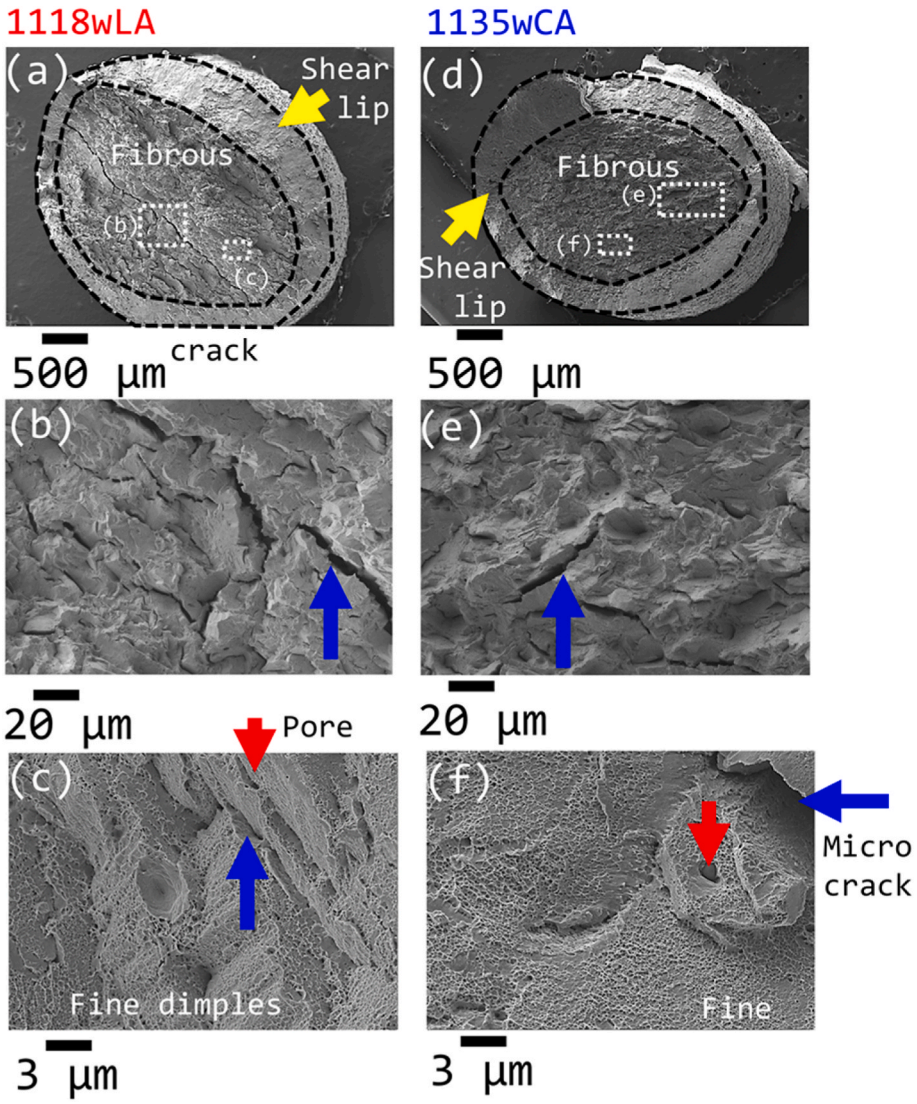

Fig. 7. A uniaxial tensile fracture surfaces of L-PBF Haynes 282 treated under a low temperature heat treatment, i.e., *1118wLA* in (a)–(c) and conventional treatment, i.e., *1135wCA* in (d)–(f). Blue arrows indicate microcracks, yellow arrows indicate shear lips. (For interpretation of the references to colour in this figure legend, the reader is referred to the Web version of this article.)

after each heat treatment step.

As confirmed by EDS analysis, the nano-sized pores and γ' precipitates in the BSE micrographs can be distinguished from the carbides by their collective characteristics in image contrast, composition, and morphology. The nano-sized pores are present as small, dark, and circular features (as indicated by white arrows in Fig. 9), which are typically decorated with brighter boundaries due to the edge charging effect. They also give out very weak x-ray signals under the EDS scans. The γ′ precipitates (as indicated by yellow and green arrows in Fig. 9), on the other hand, can appear in both bright or dark contrast. When appearing in dark contrast, they are generally lighter as compared with nano pores. In addition, γ′ phases appear as both circular and square shapes. Their composition is rich in Ni, Al, and Ti in the EDS scans, are shown in Fig. 5 (d), (i) and (j), respectively.

The unique bimodal microstructure from the low temperature treated (such as *1118wLA*) specimens originated from the beginning of the first aging step. As shown in Fig. 9(c), relatively small γ′-clusters (~40 nm or smaller) were initially formed upon heating to the first step of aging at 979 °C. The nucleation of these clusters likely had occurred at lower temperatures where the larger undercooling increased the nucleation rate [47], note that the γ′-solvus temperature is ~997 °C [10]. Some of these clustered experienced limited growth at the higher temperature portion of the heating stage. The limited nucleation and growth of γ′ was possible due to the slow heating rate (~4 °C/min) and the extended heating time. In comparison, the *1135wCA* specimens after fast heat-up (20 °C/min) to the first step aging temperature at 1010 °C (see Fig. 9(d)) did not form such clusters. Further for *1118wLA* specimens during 2 h of aging at 979 °C, due to limited degree of undercooling (~20 °C below solvus), the transformation to γ′ was expected to be mostly characterized by the growth of γ′-clusters rather than their nucleation. The growth was controlled by the diffusion of γ′-forming element from either solid solution or from smaller clusters by Ostwald ripening mechanism [48] (see Fig. 9(e), where relatively large precipitates > ~50 nm are evident). This size was consistent with the "γ′ precipitate size – Temperature – Holding time" (or "Time--Temperature-Precipitation") map reported in literature for wrought Haynes 282 [49]. However, in the *1135wCA* specimens, upon 2 h of isothermal aging at 1010 °C (which is above the γ′-solvus temperature), still there is no sign of γ′-precipitates forming (see Fig. 9(f)).

For the *1118wLA* treatment, the slow cooling (at a rate of ~2.8 °C/min) to the second aging step permitted additional time for both the larger precipitates and smaller clusters formed during first aging step to

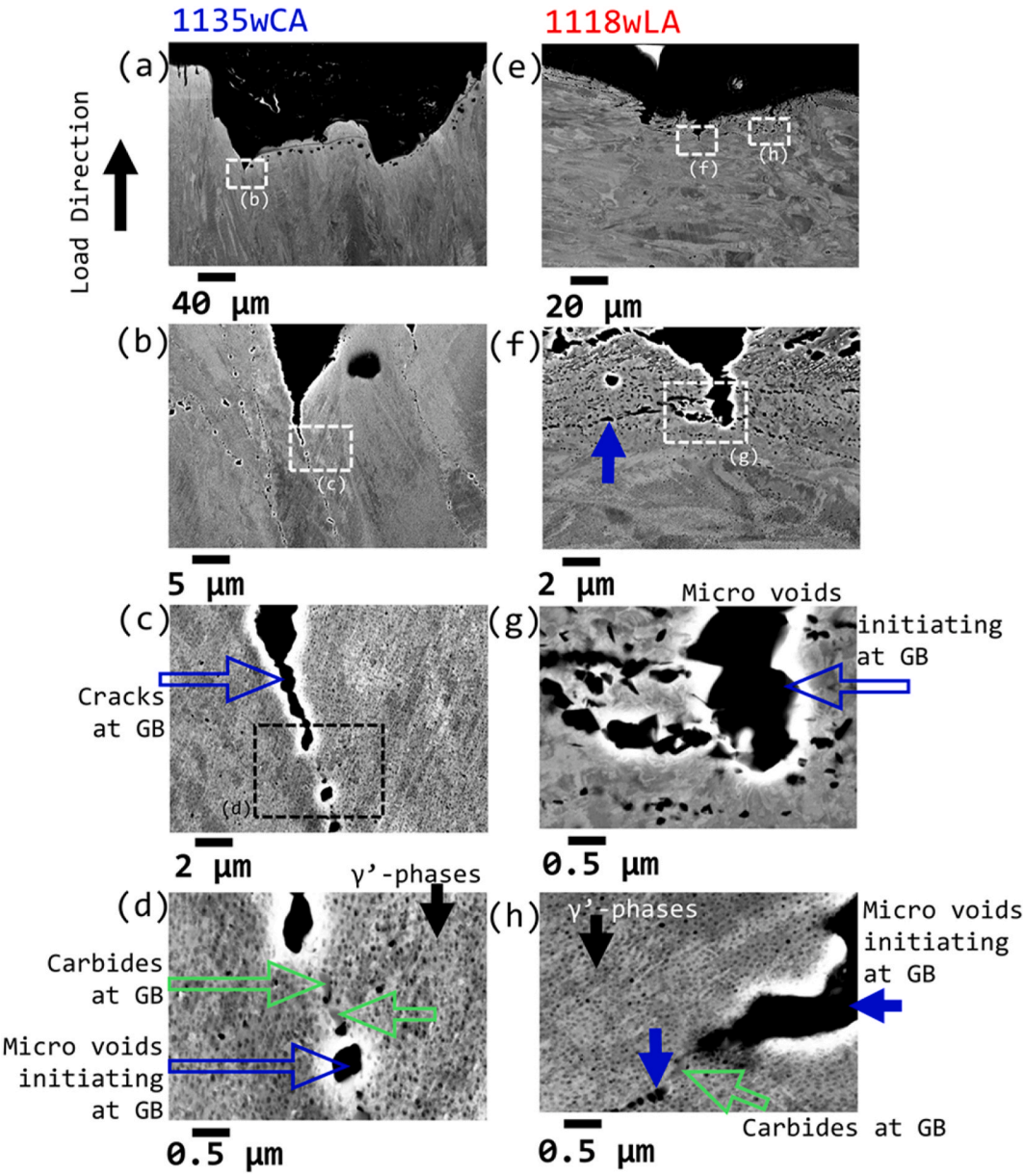

Fig. 8. Typical BSE images of the longitudinal cross sections of tensile fracture surfaces of L-PBF Haynes 282 processed by the conventional heat treatment, i.e., *1135wCA*, in (a)–(d) and by the low temperature heat treatment, i.e., *1118wLA*, in (e)–(f). Note the red arrows indicate pores, blue arrow pointed at micro voids/cracks, white arrows refer to carbide phases and black arrows show the gamma prime precipitates. (For interpretation of the references to colour in this figure legend, the reader is referred to the Web version of this article.)

grow (see Fig. 9(g)). The growth likely had slowed near the target of 757 °C due to the more sluggish diffusion at this temperature. As shown, the larger γ'-precipitates are about 150 nm in diameter, while size of the smaller γ'-precipitates are about 30 nm. On the other hand, in the *1135wCA* treated specimens, nucleation and initial growth of γ' precipitates occurred during the faster cooling (at a rate of 8 °C/min) interval between the two aging steps forming spherical *unimodal* γ'-precipitates with a uniform size of 59 ± 11 within γ-grains (see Fig. 9 (h)).

As expected, the γ'-precipitates/clusters, formed in the *1118wLA* specimens during the first step of aging at 979 °C (see Fig. 9(c)), act as precursors for formation of the larger γ'-precipitates during the subsequent slow cooling interval between the two aging steps and the following isothermal holding at 757 °C for 8 h, as shown in Fig. 9(i). By the conclusion of the *1118wLA* treatment, the sizes of these precipitates appear to fall on two ranges, i.e., ~120 nm and ~20 nm. It is also evident that many much smaller precipitates with size well below 20 nm have also formed (indicated by green dashed arrows in Fig. 9(i)). These secondary precipitates typically form at lower aging temperatures due to the higher undercooling and more sluggish diffusion, thus the phase transformation being dominated by nucleation instead of growth [47]. Thus, the resulting combination of primary γ′-precipitates with larger sizes and much smaller secondary precipitates constitute a bimodal γ′-precipitates. In addition, for *1118wLA* specimens, the number density of the larger primary γ'-precipitates in the bimodal γ′-precipitates seems to be increasing at the cost of smaller primary γ'-precipitates as the result of the second aging step (see Fig. 9(i)). This could reasonably be ascribed to Oswald ripening where the former are growing at the expense of the latter [50]. Similar bimodal γ'-precipitates have been observed in wrought Haynes 282 as the result of low temperature aging (first step aging at 996 °C followed by furnace cooling to the conventional second aging at 788 °C and 8 h of isothermal holding) [12], and the reported

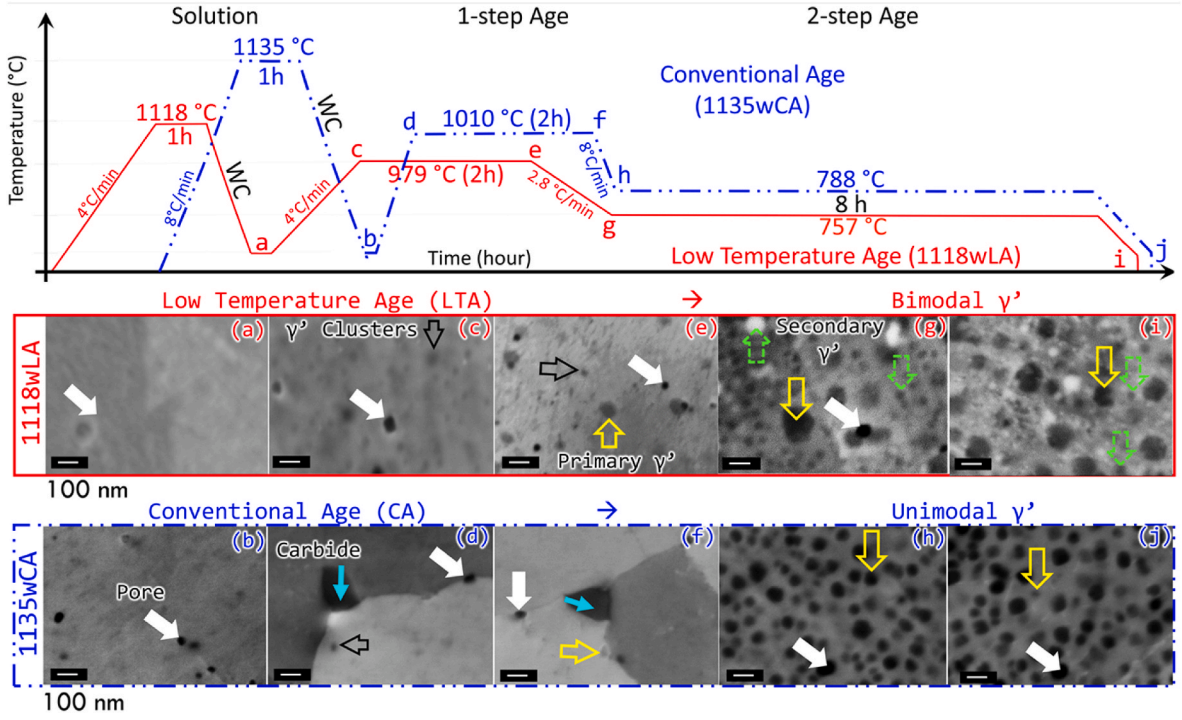

Fig. 9. Typical BSE-SEM micrographs showing microstructural evolution of L-PBF Haynes 282 during various stages of a low temperature heat treatment (*1118wLA*) in (a), (c), (e), (g), and (i) alongside with those of the conventional heat treatment (*1135wCA*) in (b), (d), (f), (h) and (j). Yellow arrows indicate primary γ' precipitates, green arrows indicate secondary ones, white arrows indicate pores, cyan arrows indicate carbides. (For interpretation of the references to colour in this figure legend, the reader is referred to the Web version of this article.)

size of the secondary γ'-precipitates are slightly larger in size (~50 nm) as compared with the present study.

In the *1135wCA* specimens, the size of the γ'-precipitates does not show a significant increase during isothermal holding of the second step of aging at 788 °C for 8 h. It is notable that the average size of the unimodal γ′-precipitates in these specimens are measured to be about 59 ± 11 nm in diameter which are comparable with what is reported in literature for the similar conventional heat treatment of both the wrought and AM Haynes 282 [30].

The bimodal γ'-microstructure offered good resistance to the motion of dislocations at room temperature due to the closely spaced secondary γ' particles well below 20 nm, as shown by the tensile curves in Fig. 2. Given their small size, these particles should be coherent with the γ matrix, therefore the resistance they offered should primarily arise from the coherency stress field and be long-range [45]. Accordingly, the cross-slip and climb activities of dislocations at elevated temperatures are not expected to deteriorate the high temperature responses such as creep strength. This is perhaps advantageous over the unimodal microstructure at lower stress levels and 750 °C where dislocations glide and climb are known to be the governing mechanism—if the bimodal structure is stable [51].

However, under prolonged thermal exposure, the bimodal γ'-microstructure in Ni-base alloys can coarsen and may lose creep strength [52–55]. For instance, during the creep deformation of the cast IN-738 [54], a γ'-Ni-based superalloy, the γ'-particles of both sizes in the bimodal γ'-microstructure were shown to have obeyed the diffusion-controlled coarsening kinetics, i.e., the Ostwald ripening or coarsening phenomena [48]. The larger γ'-particles (~0.5 μm) in the bimodal γ'-microstructure coarsened consuming the smaller γ'-particles (~0.05 μm) until eventually the latter were completely dissolved [54]. Nevertheless, the creep properties of alloys, especially polycrystalline ones, are not only determined by the intragranular microstructures, but also strongly affected by grain morphology and GB precipitates such as carbides. Formal assessment of these properties would require wholistic considerations of all governing mechanisms which is beyond the scope of this work.

5. Conclusions

In this study, the effect of heat treatment variants with lower-than-nominal temperatures and heating/cooling rates was investigated on the microstructural characteristics and mechanical behavior of L-PBF Haynes 282 superalloy. Several solution treatments were also performed at a range of temperatures to examine their efficacy in removing the as-solidified dendritic microstructure and homogenizing the grains. The following conclusions can be drawn:

1. Primarily due to second step aging at a lower temperature (757 °C/8 h), the low temperature aging heat treatment resulted in a bimodal γ′-precipitates with the primary γ′ precipitates of about 150 nm in diameter and the secondary γ′ precipitates with the size of ~20 nm, whereas the conventional heat treatment resulted in a unimodal γ′-precipitates with the γ′-precipitates of about 60 nm in diameter.
2. The presence of the fine, secondary γ′-precipitates in the low temperature aged specimens engendered them comparable tensile strengths as the conventionally treated ones, despite them containing very coarse precipitates.
3. The fracture behaviors of both sets of specimens were similarly governed by the GB carbide nucleated voids and cracks, which explains the similar ductility (measured by elongation to failure) among them.
4. Within the range of solution temperatures investigated (i.e., from 1062 °C to 1146 °C), an increase in temperature was shown to help dissolve the dendritic microstructure. However, the solution treatment did not significantly alter the grain size, due to the presence of grain boundary carbides which could not be dissolved.

Overall, it was found that the bimodal γ′-precipitates produced by

the low temperature variants were mainly responsible for the similar tensile properties in the low-temperature treated alloy compared to the conventionally treated ones. The findings of this study suggest that slight reductions in temperatures and heating/cooling rates during heat treatment—possibly due to larger component size—does not lead to significant penalties in the mechanical properties of L-PBF Haynes 282, which is partially due to the unique response of this alloy to such perturbations.

CRediT authorship contribution statement

Reza Ghiaasiaan: Conceptualization, Methodology, Investigation, Validation, Formal analysis, Investigation, Data curation, Writing – original draft, Visualization. **Nabeel Ahmad:** Conceptualization, Methodology, Investigation, Formal analysis, Data curation, Writing – original draft, Visualization. **Paul R. Gradl:** Conceptualization, Methodology, Investigation, Resources, Formal analysis, Writing – review & editing, Funding acquisition. **Shuai Shao:** Conceptualization, Methodology, Investigation, Resources, Formal analysis, Investigation, Writing – review & editing. **Nima Shamsaei:** Conceptualization, Methodology, Resources, Investigation, Formal analysis, Writing – review & editing, Supervision, Project administration, Funding acquisition.

Declaration of competing interest

The authors declare that they have no known competing financial interests or personal relationships that could have appeared to influence the work reported in this paper.

Acknowledgments

This paper is based upon the work partially funded by the National Aeronautics and Space Administration (NASA) under Award #80MSFC19C0010. The authors acknowledge the helpful discussions with P. Wang, K. Kruger, and J. Caron from Haynes International. This paper describes objective technical results and analysis. Any subjective views or opinions that might be expressed in the paper do not necessarily represent the views of the National Aeronautics and Space Administration (NASA) or the United States Government.

Appendix A. Supplementary data

Supplementary data to this article can be found online at https://doi.org/10.1016/j.msea.2021.142234.

References

[1] D. Herzog, V. Seyda, E. Wycisk, C. Emmelmann, Additive manufacturing of metals, Acta Mater. 117 (2016) 371–392.
[2] N.T. Aboulkhair, M. Simonelli, L. Parry, I. Ashcroft, C. Tuck, R. Hague, 3D printing of Aluminium alloys: additive Manufacturing of Aluminium alloys using selective laser melting, Prog. Mater. Sci. 106 (2019) 100578.
[3] J.J. Lewandowski, M. Seifi, Metal additive manufacturing: a review of mechanical properties, Annu. Rev. Mater. Res. 46 (2016) 151–186.
[4] A. du Plessis, I. Yadroitsava, I. Yadroitsev, Effects of defects on mechanical properties in metal additive manufacturing: a review focusing on X-ray tomography insights, Mater. Des. 187 (2020) 108385.
[5] A. Yadollahi, N. Shamsaei, Additive manufacturing of fatigue resistant materials: challenges and opportunities, Int. J. Fatig. 98 (2017) 14–31.
[6] N. Shamsaei, A. Yadollahi, L. Bian, S.M. Thompson, An overview of Direct Laser Deposition for additive manufacturing; Part II: mechanical behavior, process parameter optimization and control, Addit. Manuf. 8 (2015) 12–35.
[7] New manufacturing milestone: 30,000 Additive Fuel Nozzles, ((n.d.)).
[8] R.G.J. Clinton, Additive Manufacturing for Human Space Exploration, 2018, p. 24.
[9] B. Blakey-Milner, P. Gradl, G. Snedden, M. Brooks, J. Pitot, E. Lopez, M. Leary, F. Berto, A. du Plessis, Metal additive manufacturing in aerospace: a review, Mater. Des. (2021) 110008.
[10] M.J. Donachie, S.J. Donachie, Superalloys: A Technical Guide, second ed., ASM International, Materials Park, OH, 2002.
[11] J. Chander, Hardening mechanism and corrosion resistance of nickel-base alloys: a review, Can. Metall. Q. 3 (1964) 57–77.
[12] C. Joseph, C. Persson, M. Hörnqvist Colliander, Influence of heat treatment on the microstructure and tensile properties of Ni-base superalloy Haynes 282, Mater. Sci. Eng. 679 (2017) 520–530.
[13] K.-Y. Shin, J.-H. Kim, M. Terner, B.-O. Kong, H.-U. Hong, Effects of heat treatment on the microstructure evolution and the high-temperature tensile properties of Haynes 282 superalloy, Mater. Sci. Eng. 751 (2019) 311–322.
[14] F.S. Yin, Q. Zheng, X.F. Sun, H.R. Guan, Z.Q. Hu, Effect of melt treatment on carbides formation in a cast nickel-base superalloy M963, J. Mater. Process. Technol. 183 (2007) 440–444.
[15] S.A. Sajjadi, S. Nategh, R.I. Guthrie, Study of microstructure and mechanical properties of high performance Ni-base superalloy GTD-111, Mater. Sci. Eng. 325 (2002) 484–489.
[16] R.M. Kearsey, J. Tsang, S. Oppenheimer, E. McDevitt, Microstructural effects on the mechanical properties of ATI 718Plus® alloy, JOM 64 (2012) 241–251.
[17] J. Saarimäki, J.J. Moverare, M.H. Colliander, Time- and cycle-dependent crack propagation in Haynes 282, Mater. Sci. Eng. 658 (2016) 463–471.
[18] L.M. Pike, Development of a fabricable gamma-prime (γ′) strengthened superalloy, Proc. Int. Symp. Superalloys. (2008) 191–200.
[19] L.M. Pike, C. Ni-cr-mo, N. Mo, 100 + YEARS OF WROUGHT ALLOY DEVELOPMENT AT HAYNES INTERNATIONAL Keywords : alloy Development , Haynes International Abstract solutions to materials problems to its customers . In return , its customers , through advancements alloys, Now Then (2014) 15–30, many ne.
[20] M. Seifi, M. Gorelik, J. Waller, N. Hrabe, N. Shamsaei, S. Daniewicz, J. J. Lewandowski, Progress towards metal additive manufacturing standardization to support qualification and certification, JOM 69 (2017) 439–455.
[21] Haynes Internatioal Website, Haynes 282 Alloy: Principal Features, (n.d).
[22] Astm International, ASTM B637-18 Standard Specification for Precipitation-Hardening and Cold Worked Nickel Alloy Bars, Forgings, and Forging Stock for Moderate or High Temperature Service, ASTM B. Stand., 2018.
[23] K.A. Unocic, M.M. Kirka, E. Cakmak, D. Greeley, A.O. Okello, S. Dryepondt, Evaluation of additive electron beam melting of haynes 282 alloy, Mater. Sci. Eng. 772 (2020) 138607.
[24] M. Kirka, K. Unocic, K. Kruger, A. Forsythe, Process Development for Haynes® 282® Using Additive Manufacturing, 2018.
[25] Astm B637 - 12 ASTM B637 - 12-Standard Specification for Precipitation-Hardening and Cold Worked Nickel Alloy Bars, Forgings, and Forging Stock for Moderate or High Temperature Service, ((n.d.)).
[26] AMS5951, AMS5951 - aerospace material specification, Aerosp. Mater. Specif. (2017).
[27] R. Snell, S. Tammas-Williams, L. Chechik, A. Lyle, E. Hernández-Nava, C. Boig, G. Panoutsos, I. Todd, Methods for rapid pore classification in metal additive manufacturing, JOM 72 (2020) 101–109.
[28] J.W. Pegues, S. Shao, N. Shamsaei, N. Sanaei, A. Fatemi, D.H. Warner, P. Li, N. Phan, Fatigue of additive manufactured Ti-6Al-4V, Part I: the effects of powder feedstock, manufacturing, and post-process conditions on the resulting microstructure and defects, Int. J. Fatig. 132 (2020) 105358.
[29] S. Liu, Y.C. Shin, Additive manufacturing of Ti6Al4V alloy: a review, Mater. Des. 164 (2019) 107552.
[30] K.A. Unocic, D. Shin, X. Sang, E. Cakmak, P.F. Tortorelli, Single-step aging treatment for a precipitation-strengthened Ni-based alloy and its influence on high-temperature mechanical behavior, Scripta Mater. 162 (2019) 416–420.
[31] A. Ramakrishnan, G.P. Dinda, Microstructure and mechanical properties of direct laser metal deposited Haynes 282 superalloy, Mater. Sci. Eng. 748 (2019) 347–356.
[32] A. Ramakrishnan, G.P. Dinda, Functionally graded metal matrix composite of Haynes 282 and SiC fabricated by laser metal deposition, Mater. Des. 179 (2019) 107877.
[33] V. Pettersson, Study of the Effect of Process Parameters in Laser Blown Powder with Superalloys, 2018.
[34] K.A. Christofidou, H.T. Pang, W. Li, Y. Pardhi, C.N. Jones, N.G. Jones, H.J. Stone, Microstructural control and optimization of haynes 282 manufactured through laser powder bed fusion, in: A.S. Sammy Tin, Mark Hardy, Justin Clews, Jonathan Cormier, Qlang Feng, John Marcin, Chris O'Brien (Eds.), Superalloys 2020, Springer International Publishing, 2020, pp. 1014–1023.
[35] A. Deshpande, S. Deb Nath, S. Atre, K. Hsu, Effect of post processing heat treatment routes on microstructure and mechanical property evolution of haynes 282 Ni-based superalloy fabricated with selective laser melting (SLM), Metals 10 (2020) 629.
[36] A.S. Shaikh, F. Schulz, K. Minet-Lallemand, E. Hryha, Microstructure and mechanical properties of Haynes 282 superalloy produced by laser powder bed fusion, Mater. Today Commun. 26 (2021) 102038.
[37] E.8 Astm, ASTM E8/E8M standard test methods for tension testing of metallic materials 1, Annu. Book ASTM Stand. 4 (2010) 1–27.
[38] Astm International, ASTM E3-11: Standard Guide for Preparation of Metallographic Specimens, 2012.
[39] S. Zaefferer, N.-N. Elhami, Theory and application of electron channelling contrast imaging under controlled diffraction conditions, Acta Mater. 75 (2014) 20–50.
[40] SAE International, AMS 5951, 2010.
[41] Astm International, ASTM E112-10: Standard Test Methods for Determining Average Grain Size, 2010.
[42] T.P. Gabb, J. Telesman, A. Banik, E. McDevitt, Use of slow strain rate tensile testing to assess the ability of several superalloys to resist environmentally-assisted intergranular cracking, 8th Int. Symp. Superalloy 718 Deriv (2014) 697–712, 2014.
[43] M.R. Ahmadi, M. Rath, E. Povoden-Karadeniz, S. Primig, T. Wojcik, A. Danninger, M. Stockinger, E. Kozeschnik, Modeling of precipitation strengthening in Inconel

718 including non-spherical γ ″ precipitates, Model. Simulat. Mater. Sci. Eng. 25 (2017), 055005.
[44] T.G. Gallmeyer, S. Moorthy, B.B. Kappes, M.J. Mills, B. Amin-Ahmadi, A. P. Stebner, Knowledge of process-structure-property relationships to engineer better heat treatments for laser powder bed fusion additive manufactured Inconel 718, Addit. Manuf. 31 (2020) 100977.
[45] M.A. Meyers, K.K. Chawla, Mechanical Behavior of Materials, second ed., Cambridge University Press, Cambridge, 2009.
[46] G.E. Dieter, Mechanical Metallurgy, 2011.
[47] D.A. Porter, K.E. Easterling, Phase Transformations in Metals and Alloys, Springer US, Boston, MA, 1992.
[48] A. Baldan, Review Progress in Ostwald ripening theories and their applications to the γ′-precipitates in nickel-base superalloys Part II Nickel-base superalloys, J. Mater. Sci. 37 (2002) 2379–2405.
[49] K. Vattappara, Understanding the Effect of Temperature and Time on Gamma Prime Coarsening for Nickel-Base Superalloy Haynes 282, KTH Royal Institute of Technology, 2019.
[50] A. Baldan, Review Progress in Ostwald ripening theories and their applications to nickel-base superalloys Part I: Ostwald ripening theories, J. Mater. Sci. 37 (2002) 2171–2202.
[51] X. Song, L. Tang, Z. Chen, R. Zhou, Micro-mechanism during long-term creep of a precipitation-strengthened Ni-based superalloy, J. Mater. Sci. 52 (2017) 4587–4598.
[52] Z. Peng, G. Tian, J. Jiang, M. Li, Y. Chen, J. Zou, F.P.E. Dunne, Mechanistic behaviour and modelling of creep in powder metallurgy FGH96 nickel superalloy, Mater. Sci. Eng. 676 (2016) 441–449.
[53] J. ZRNÍK, V. Vrchovinský, Heat treatment structure modification of wrought nickel based superalloy and its creep resistance, J. Phys. IV 3 (1993). C7-C283-C7-288.
[54] R.A. Stevens, P.E.J. Flewitt, The effects of γ′ precipitate coarsening during isothermal aging and creep of the nickel-base superalloy IN-738, Mater. Sci. Eng. 37 (1979) 237–247.
[55] J. Coakley, D. Dye, H. Basoalto, Creep and creep modelling of a multimodal nickel-base superalloy, Acta Mater. 59 (2011) 854–863.